energies

MDPI

Article

Plate–Fin Heat Exchanger Study: Performance Prediction and Optimization Using PSO-BP-ANN Model

Xinyue Duan [1], Yanlong Zhang [1], Zhaowen Hao [1], Liang Gong [1,*], Lande Liu [2] and Chuanyong Zhu [1]

[1] College of New Energy, China University of Petroleum (East China), Qingdao 266580, China; duanxy@upc.edu.cn (X.D.); 18764773305@163.com (Y.Z.); 13854598662@163.com (Z.H.); cyzhu@upc.edu.cn (C.Z.)
[2] School of Applied Sciences, University of Huddersfield, Queensgate, Huddersfield HD1 3DH, UK; l.liu@hud.ac.uk
* Correspondence: lgong@upc.edu.cn

Abstract

Plate–fin heat exchangers (PFHEs) are widely used in petrochemical, energy and electric power, aerospace, and other industries with large heat transfer requirements. The development of performance prediction and optimization methods for PFHEs has become increasingly important in the design and operation of such heat exchangers (HEs). This paper establishes a database of flow and heat transfer characteristics for four types of PFHEs with different structural parameters. Based on this database, the back-propagation artificial neural network (BP-ANN) model was optimized using the particle swarm optimization (PSO) algorithm to form the PSO-BP-ANN model for the performance prediction of these four types of PFHEs. This combination has been found to improve the prediction accuracy and generalization ability of the BP-ANN model. Additionally, the non-dominated sorting genetic algorithm II (NSGA-II) method was used to characterize the relationship between four structural parameters to be optimized (the length, height, spacing, and thickness of the HE fin) and the two objective functions (j and f) of the serrated PFHE in laminar flow. This enables the Pareto optimal solution to be obtained. The results show that, under laminar flow conditions (Re = 800), the serrated fin HE achieves the best heat transfer performance when the fin height, spacing, thickness, and length are 9.29, 1.22, 0.16, and 3.06, respectively.

Keywords: plate–fin heat exchanger; PSO-BP-ANN; pareto; NSGA-II; multi-objective optimization

Check for updates

Academic Editor: Artur Blaszczuk

Received: 28 April 2026
Revised: 29 June 2026
Accepted: 30 June 2026
Published: 5 July 2026

Copyright: © 2026 by the authors. Licensee MDPI, Basel, Switzerland. This article is an open access article distributed under the terms and conditions of the Creative Commons Attribution (CC BY) license.

1. Introduction

The worldwide demand for energy saving and carbon reduction has pushed the traditional energy industry to pursue higher efficiency. Meanwhile, with the rapid rise of Internet of Things technology, intelligent heat exchangers (HEs) have emerged. Plate–fin heat exchangers (PFHEs) are widely used in areas such as petrochemical, energy and power, marine engineering and aerospace, etc. [1]. The core component that determines the flow and heat transfer performance of a PFHE is the plate bundle. It is fabricated by brazing fins and deflectors together, and it comes in various structural types. Common plate–fin structures include straight fins, wavy fins, serrated fins, porous fins, and louvered fins [2]. Therefore, it is extremely important to develop performance prediction and optimization methods for the design and manufacture of PFHEs.

PFHEs usually rely on existing empirical correlations for performance prediction and optimal design [3]. These correlations are obtained from experiments or numerical

simulations. However, they are limited by the structure of the HE and the type of working fluid, and some predicted data exhibit large errors [4]. In recent years, machine learning algorithms (MLAs) have broken through the technical bottlenecks of the above methods. Owing to their fast convergence and high accuracy, MLAs have gradually become a research hotspot [5,6]. In 2003, Islamoglu [7] established an artificial neural network (ANN) model to predict the heat transfer rate of heat exchangers (HEs) and discussed the feasibility and applicability of ANN in the field of HEs. Zhao [8] also pointed out that the heat transfer coefficient of an HE depends on the physical properties of the working fluid at different operating pressures and temperatures. Nonetheless, ANN is more flexible and adaptable in dealing with such complex nonlinear problems.

The BP-ANN method is based on the error back-propagation algorithm, which gradually adjusts the network parameters to better fit the training data, and it has attracted attention in the performance prediction of HEs [9]. Peng and Ling [10] used this method to establish a prediction model for the j and f factors of five PFHE channels; the mean square errors between the predicted and experimental values were less than 1.5% and 1%, respectively. Based on the same method, Dong and Du [11] found that the BP-ANN model is easily affected by the choice of initial parameters and data distribution, and tends to fall into a local optimum.

In view of the above problems, the Genetic Algorithm (GA) is used to improve the global search and local optimization capability of the BP-ANN model. However, studies have shown that GA-BP-ANN suffers from high computational complexity and difficulties in parameter selection, which ultimately slows down computation. To further optimize the prediction model, Zhao et al. [12] introduced Particle Swarm Optimization (PSO) to optimize the weights and thresholds of the BP-ANN model. Not only does this make global search possible, but it also prevents the model from falling into a local optimum due to premature convergence, thereby avoiding large deviations in some predicted values and other consequent problems [13]. Wang et al. [14] established a prediction model for HE channels and compared the prediction results before and after PSO. They found that the mean squared errors for Nu and f obtained after PSO were reduced by 56.8% and 95.2%, respectively. In summary, in the engineering design of HEs, the PSO-BP-ANN model offers unique advantages, such as global search capability, fast training, high precision, and strong generalization ability.

How to design a heat exchanger with high efficiency and low energy consumption to achieve the engineering goals of enhancing heat transfer and reducing flow resistance is an important issue [15,16]. Segundo et al. [17] proposed the Falcon optimization algorithm and applied it to the single-objective and multi-objective optimization of PFHEs. Wang et al. [18] successfully used the genetic algorithm for multi-objective optimization; the maximum performance evaluation criterion (PEC) and the maximum field coordination number (Fc) were used as two objective functions to optimize the structure of the convex heat exchanger. The results showed that the optimized structure could significantly improve the comprehensive heat transfer performance of the convex heat exchanger. Lv et al. [19] combined machine learning and NSGA-II to study the influence of different design variables on the friction coefficient, PEC, and entropy production (S) of PCHE. The TOPSIS decision-making method was used to select the optimal solution from the Pareto frontier. Compared with the original situation, the optimal situation increased the PEC by 8.5% and reduced the S value by 9.98%. He et al. [20] studied PFHEs by combining NSGA-II with an ANN model. They took minimizing the heat source mean temperature and minimizing the pressure drop as the objective functions to optimize the fin geometry and maximize its overall performance, and they obtained an acceptable optimization solution. Wang et al. [14] considered airfoil fin PFHEs and combined the NSGA-II and PSO-BP-ANN models to

optimize the fin arrangement parameters. They achieved a 113.25% reduction in the friction factor f at the expense of a 10.29% reduction in Nu. Yang et al. [21] combined the sensitivity analysis method with NSGA-II to predict and optimize the structural parameters of serrated fin PFHEs. Studies have shown that NSGA-II combined with the PSO-BP-ANN model can provide parameter optimization guidance for the development of green and high-efficiency HEs [22], but it has not received sufficient attention or been widely applied in HE optimization.

Therefore, this study develops a data-driven prediction and optimization framework for PFHE fin channels. Empirical correlations are useful for engineering calculations, but their applicability is often limited by the tested geometry, working fluid, and operating range. For fin channels with different structural parameters, the relationship between geometry and the j and f factors is nonlinear, and the use of a single correlation may lead to inconsistent prediction results. In this context, BP-ANN is used to learn the mapping between fin-channel parameters and thermal–hydraulic performance, while PSO is introduced to reduce the influence of initial weights and thresholds on the ANN prediction. Since heat transfer enhancement and flow resistance reduction are competing requirements, the optimized PSO-BP-ANN model is further coupled with NSGA-II to identify a reasonable compromise for serrated fin design within the database range.

2. Database Establishment

In this paper, the heat transfer and flow resistance performance database of the fin channels of four types of PFHEs using air as the working fluid is established through the literature data [23–35] and numerical simulation (see Appendix A for details). The database provides supporting data for the subsequent development of a performance prediction model for the heat exchangers. The four types of PFHEs are shown in Figure 1, and their main structural parameters and performance data sources are shown in Table 1. Here, the dimensionless parameters to assess heat transfer efficiency and fluid flow resistance are defined as j factor and f factor, respectively.

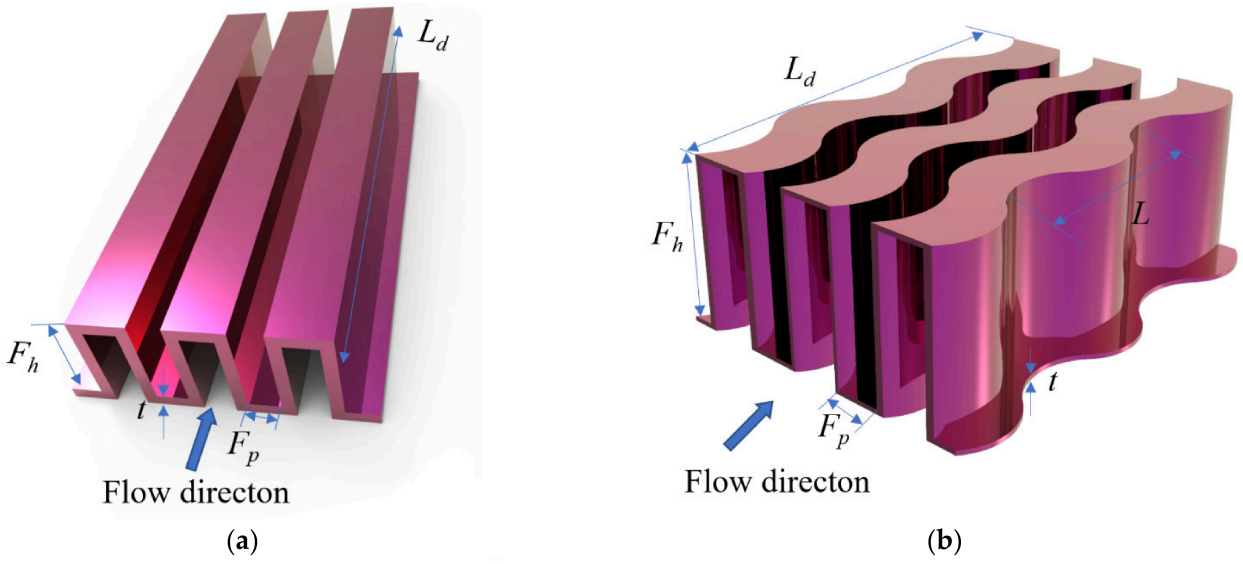


Figure 1. *Cont.*

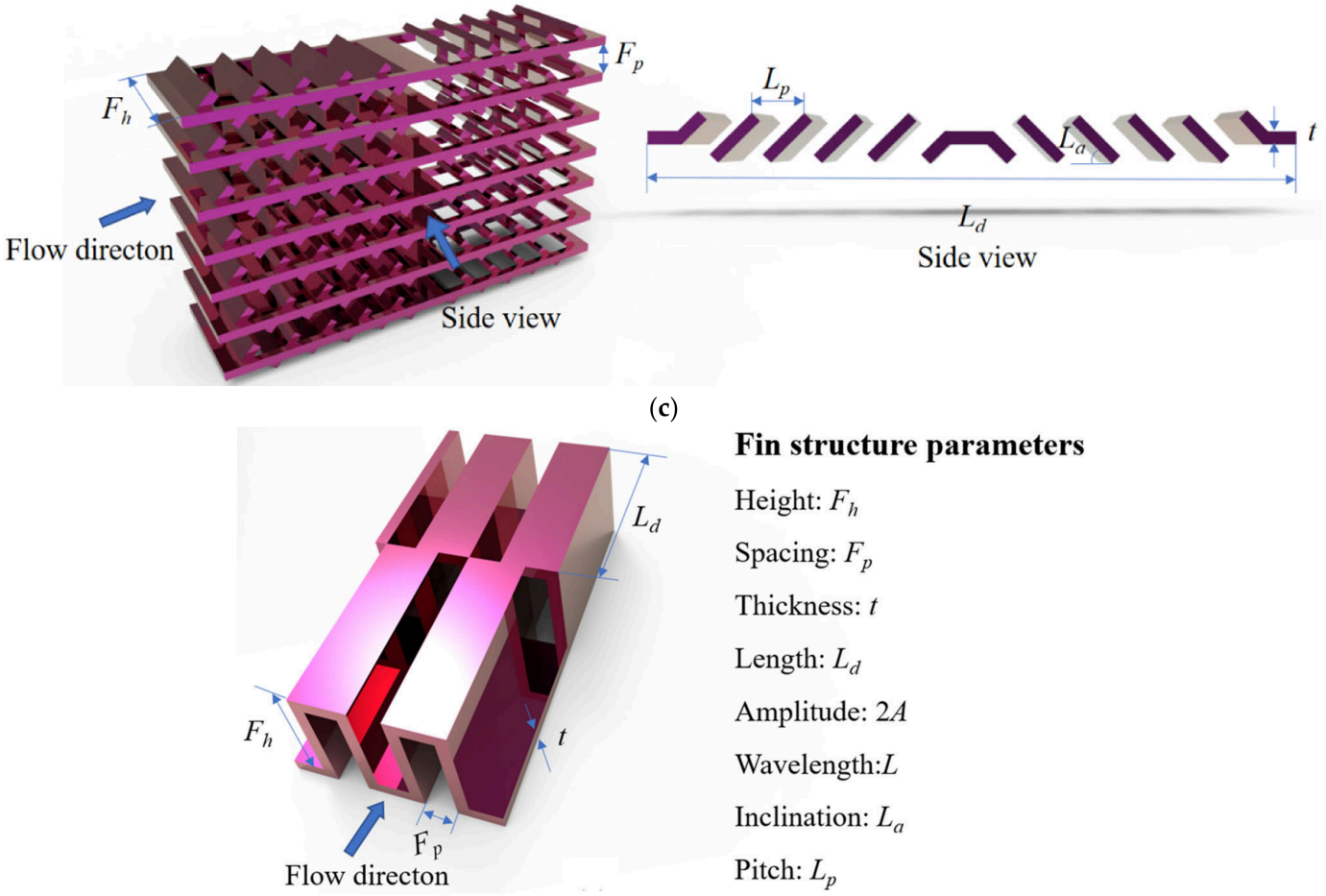


Figure 1. Schematic structure diagram of PFHEs: (**a**) straight fin; (**b**) wavy fin; (**c**) louver fin; (**d**) serrated fin.

Table 1. Main structural parameters and performance data sources.

Fin Type	Data Sources	Main Structural Parameters	Performance Parameters	Amount of Data
Straight fin	Dong et al. [24] Kays and London [23]	F_p, F_h, t, L_d	J, f	880
Wavy fin	Aliabadi et al. [27] Dong et al. [26] Naef et al. [28] Kays and London [23] Gough and Shemmeri [25]	F_p, F_h, t, L_d, $2A$, L	J, f	1056
Louver fin	Kim et al. [33] Dong et al. [34] Chang and Wang [29–32]	F_p, F_h, t, L_d, L_a, L_p	J, f	4166
Serrated fin	Dong et al. [34] Kays and London [23] Peng and Ling [35]	F_p, F_h, t, L_d	J, f	1179

Table 2 presents the Chinese standard for aluminum plate–fin heat exchangers. Song et al. [36] showed that the existing correlations in the literature yield significant errors when predicting the performance of Chinese serrated fin channels. To obtain a broader set of

performance data, we will supplement the data for domestic serrated fin channels through numerical simulation.

Table 2. Structural parameters of domestic serrated fins.

Surface	F_h/mm	F_p/mm	t/mm	L_d/mm	α	γ	δ
95JC1402	9.3	1.2	0.2	5	0.129	0.167	0.040
95JC1702	9.3	1.5	0.2	5	0.161	0.133	0.040
95JC2002	9.3	1.8	0.2	5	0.194	0.111	0.040
65JC1703	6.2	1.4	0.3	5	0.226	0.214	0.060
65JC2003	6.2	1.7	0.3	5	0.274	0.176	0.060
47JC2003	4.4	1.7	0.3	5	0.386	0.176	0.060
30JC3503	2.7	3.2	0.3	5	1.185	0.094	0.060

The solid material of the serrated fin channels is aluminum, and the working fluid is air. The physical properties of air are shown in Table 3.

Table 3. The physical properties of air.

ρ (kg/m^3)	C_p (J/kg·K)	λ (W/m·K)	μ (Pa·s)
1.165	1005	0.0267	1.86×10^{-5}

To improve computational efficiency, a steady-state model is adopted in this study, with the following assumptions:

(1) The fluid in the channel is incompressible and undergoes no phase change.
(2) The working medium is single-phase dry air, and its thermophysical properties remain constant.
(3) The effects of thermal radiation and natural convection can be neglected during the flow.

In this section, ANSYS Fluent 17.0 is used to analyze the flow and heat transfer characteristics of the serrated fin channel. The continuity, momentum, and energy equations are given as follows:

$$\frac{\partial}{\partial x_i}(\rho u_i) = 0 \tag{1}$$

$$\frac{\partial}{\partial x_j}(\rho u_i u_j) = \frac{\partial}{\partial x_j}\left(\mu \frac{\partial u_i}{\partial x_j}\right) - \frac{\partial p}{\partial x_i} \tag{2}$$

$$\frac{\partial}{\partial x_j}(\rho u_j T) = \frac{\partial}{\partial x_j}\left(\frac{\mu}{Pr}\frac{\partial T}{\partial x_j}\right) \tag{3}$$

The serrated fin channel model in this study should ensure that the ratio of flow length to hydraulic diameter is greater than 60. To prevent backflow, the lengths of both the inlet and outlet extension sections are each 20 times the hydraulic diameter. The calculation method for the inlet velocity of the extension section is as follows:

$$u_{in}A_{in} = uA_c \tag{4}$$

where u is the velocity at the fin inlet, u_{in} is the velocity at the extension section inlet, A_c is the cross-sectional area of the fin, and A_{in} is the cross-sectional area of the extension section inlet.

The inlet face is set as a velocity inlet, and the outlet face as a pressure outlet. The inlet air temperature is 300 K, and the temperatures of the upper and lower parting sheets are 373.15 K. Periodic boundary conditions are applied to the left and right sides of the channel. For $300 \leq Re < 1000$, the laminar model is used; for $Re > 1000$, the SST k-ω turbulence model is employed. The transport equations for the turbulent kinetic energy k and the dissipation rate ω are respectively given as follows:

$$\frac{\partial}{\partial x_i}(\rho k u_i) = \frac{\partial}{\partial x_j}\left(\Gamma_k \frac{\partial k}{\partial x_j}\right) + G_k \tag{5}$$

$$\frac{\partial}{\partial x_i}(\rho \omega u_i) = \frac{\partial}{\partial x_j}\left(\Gamma_\omega \frac{\partial \omega}{\partial x_j}\right) + G_\omega \tag{6}$$

The pressure-velocity coupling is handled by the SIMPLE algorithm, and the second-order upwind scheme is adopted for the energy and momentum equations. The solution is considered converged when the computational residuals fall below 10^{-6}. The computational model is meshed with structured grids generated by ICEM software 19.0. Boundary layer grids are applied near the walls and locally refined. A schematic of the mesh is shown in Figure 2.

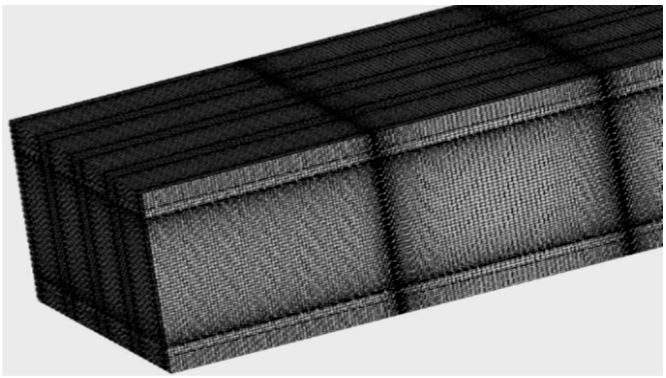


Figure 2. Schematic diagram of serrated fin grid.

Figure 3 shows the grid independence verification for the 47JC2003 fin channel at Re = 800. The variations in both the heat transfer factor and the friction factor between the results obtained from the third and fourth sets of grids are less than 1%. To balance numerical accuracy and computational cost, a grid number of 3,626,320 is selected for the 47JC2003 fin channel. The grid numbers for all the serrated fin channels of the plate–fin heat exchangers in this study range from 2,519,130 to 8,296,832.

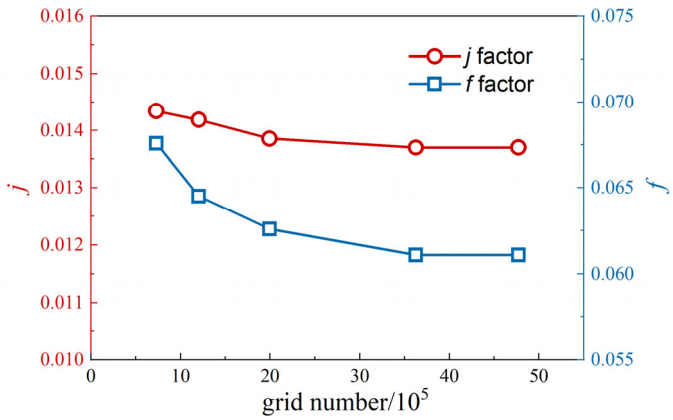


Figure 3. Grid independence verification diagram.

To verify the accuracy of the numerical simulation, the computed values are compared with the experimental data from reference, and the results are shown in Figure 4. As can be seen from Figure 4, the numerically simulated j and f factors agree well with the experimental values, with mean absolute percentage errors of 8.07% and 9.28%, respectively. Therefore, the numerical simulation results are considered reliable.

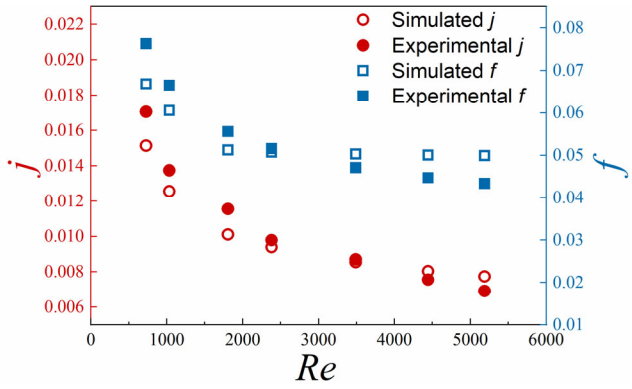


Figure 4. Comparison of numerical simulation and experimental results.

Within the range of serrated fin geometries both domestic and international, four structural parameters were uniformly selected according to the rules of orthogonal experiments. The structural parameters of the serrated fins are listed in Table 4. Performance data of 25 serrated fin channels were obtained through numerical simulation and randomly mixed with literature data to expand the serrated fin channel database.

Table 4. Design Points for Orthogonal Experiments.

Number	F_h/mm	F_p/mm	t/mm	L_d/mm
1	2.7	1.2	0.1	3
2	2.7	1.7	0.3	7.5
3	2.7	2.2	0.5	4.5
4	2.7	2.7	0.2	9
5	2.7	3.2	0.4	6
6	4.35	1.2	0.5	7.5
7	4.35	1.7	0.2	4.5
8	4.35	2.2	0.4	9
9	4.35	2.7	0.1	6
10	4.35	3.2	0.3	3
11	6	1.2	0.4	4.5
12	6	1.7	0.1	9
13	6	2.2	0.3	6
14	6	2.7	0.5	3
15	6	3.2	0.2	7.5
16	7.65	1.2	0.3	9
17	7.65	1.7	0.5	6
18	7.65	2.2	0.2	3
19	7.65	2.7	0.4	7.5
20	7.65	3.2	0.1	4.5
21	9.3	1.2	0.2	6
22	9.3	1.7	0.4	3
23	9.3	2.2	0.1	7.5
24	9.3	2.7	0.3	4.5
25	9.3	3.2	0.5	9

3. Machine Learning Model Establishment

3.1. Sample Data Preprocessing

Before training the model, the input data need to be normalized to eliminate the differences in magnitude among the sample variables and to balance the influence of each parameter on the model prediction. At the same time, normalization can map the data into a region where the activation function has a large gradient, thereby preventing neurons from having zero gradients during training. As shown in Equations (7) and (8), the data are normalized (and denormalized) to fall within the range [0.15, 0.85]. Separate models were trained independently for each fin type. For each dataset, 85% of the data were used for training and the remaining 15% for testing. For the serrated fin channel, the 25 additional CFD cases were merged with the literature data before the dataset was split into training and testing sets.

$$P_n = \frac{P_m - P_{min}}{P_{max} - P_{min}}(S_{max} - S_{min}) + S_{min} \tag{7}$$

$$P_m = \frac{P_n - S_{min}}{S_{max} - S_{min}}(P_{max} - P_{min}) + P_{min} \tag{8}$$

In Equations (7) and (8), S_{max} and S_{min} are 0.85 and 0.15, respectively; P_{max} and P_{min} are the maximum and minimum values of input variables; P_n and P_m are the normalized data and denormalized data, respectively.

3.2. Establish PSO-BP-ANN Prediction Model

3.2.1. Establish BP-ANN Model

The BP-ANN prediction models established in this paper adopt a three-layer neural network structure, and the schematic diagram is shown in Figure 5. The input parameters and their upper and lower limits for the HE channels are listed in Table 5. A separate prediction model was established for each fin-channel type because the geometric variables and their dimensionless input forms differ among the straight, wavy, louvered, and serrated fins. The limits listed in Table 5 define the input range of each corresponding model, and the prediction results should be interpreted within these ranges. As can be seen from Table 5, the performance of PFHEs is greatly affected by the cross-sectional shape of the channel. Following the correlation-based approach, the corresponding dimensionless parameters are adopted as the input parameters. Through iterative training and tuning, the optimal configuration of the activation function, training algorithm, learning rate, and number of hidden-layer neurons is determined, as shown in Table 6. During training, the same training and test sets are maintained, and the coefficient of determination (R^2), root mean square error (*RMSE*), and mean absolute percentage error (*MAPE*) on the test set are chosen as evaluation metrics [37–39].

$$R^2 = 1 - \left(\frac{\sum_{i-1}^{n} (t_i - o_i)^2}{\sum_{i-1}^{n} (o_i)^2} \right) \tag{9}$$

$$RMSE = \sqrt{\frac{1}{n} \sum_{i=1}^{n} (t_i - o_i)^2} \tag{10}$$

$$MAPE = \frac{1}{n} \sum_{i=1}^{n} \left(\left| \frac{t_i - o_i}{t_i} \right| \right) \times 100\% \tag{11}$$

where t_i and o_i are the target and predicted values, respectively; n is the number of samples.

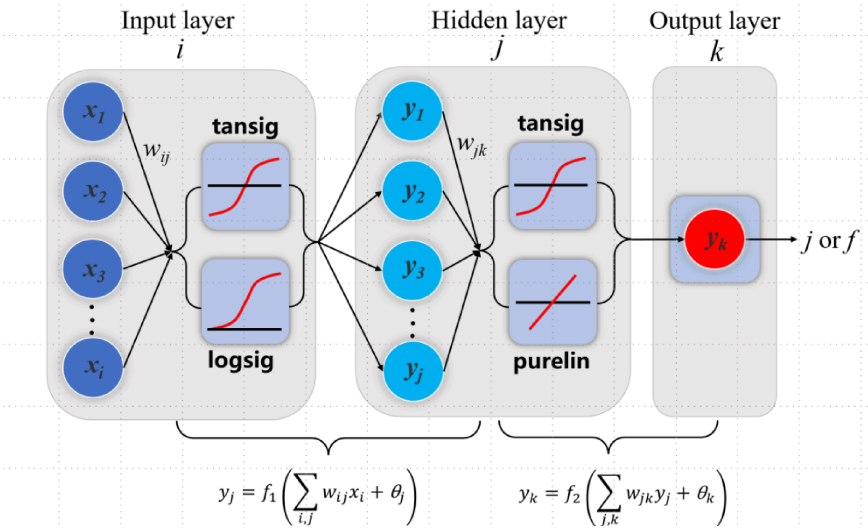


Figure 5. Basic structure diagram of BP neural network.

Table 5. Input parameters and upper and lower limits of the PFHE channels.

Name	Serial Number	Parameter	Lower Limit	Upper Limit	Name	Serial Number	Parameter	Lower Limit	Upper Limit
Straight fin	Input1	F_p/D_e	0.606	1.049	Louver fin	Input1	F_p/L_p	0.447	4.11
	Input2	F_h/D_e	1.318	7.169		Input2	F_h/L_p	2.6	16
	Input3	t/D_e	0.0247	0.132		Input3	L_d/L_p	9.41	95.6
	Input4	L_d/D_e	5.505	82.98		Input4	t/L_p	0.025	0.167
	Input5	Re	200	10,000		Input5	$L_a/90$	0.094	0.389
Wavy fin	Input1	F_p/F_h	0.025	1.625		Input6	Re	100	3000
	Input2	F_p/t	1	130	Serrated fin	Input1	F_p/F_h	0.129	1.185
	Input3	L_d/L	2	7		Input2	t/L_d	0.011	0.167
	Input4	$F_h/2A$	0.1	16.67		Input3	t/F_p	0.031	0.417
	Input5	Re	300	10,000		Input4	Re	200	10,000

Table 6. Optimal parameters of BP-ANN model for four types of PFHEs.

Content	Straight Fin		Wavy Fin		Louver Fin		Serrated Fin	
	j	*f*	*j*	*f*	*j*	*f*	*j*	*f*
Hidden layer activation function	logsig	logsig	logsig	logsig	logsig	logsig	tansig	tansig
Output layer activation function	tansig	tansig	purelin	purelin	purelin	purelin	purelin	purelin
Training algorithm	trainlm	trainlm	trainlm	trainlm	trainlm	trainlm	trainlm	trainlm
Learning rate	0.4	0.4	0.4	0.4	0.4	0.4	0.4	0.4
Number of neurons in the hidden layer	10	4	7	8	9	13	11	10

3.2.2. Particle Swarm Optimization (PSO)

In order to prevent the model from being sensitive to initialization and falling into a local optimum, this paper uses the PSO algorithm, which simulates the collective behavior of bird flocks or fish schools, to find the optimal BP-ANN parameters [40]. The process is shown in Figure 6, and the design steps are as follows:

(1) Determine the size of the particle swarm and the parameters of the algorithm. The search space has a dimension D, the number of particles is m, the inertia weight is w, and the acceleration factors are C_1 and C_2, respectively. Here, each particle is a D-dimensional vector, and the weights and thresholds of the BP-ANN are encoded into the particles, so that the particle dimension D equals the total number of weights and thresholds. The initial parameters of the PSO algorithm are set as follows: the

maximum number of evolutionary iterations is 200, the population size is 100, the inertia weight is 1, and the acceleration factors C_1 and C_2 are both 1.5. Through iterative training and tuning, the optimal parameter configuration of the model is determined, as shown in Table 7.

(2) Determine the *fitness* function. In the PSO algorithm, the *fitness* of each particle is defined as the *RMSE* of the predictions on the training set. The *fitness* value indicates the quality of the particle and is used to guide the particle swarm search. It is calculated as follows [41]:

$$fitness = \frac{1}{n}\sum_{i=1}^{n}(t_i - o_i)^2 \tag{12}$$

(3) Initialize the database and unify the data within the interval [0.15, 0.85]. The generated m particles represent m BP neural networks with different weights and thresholds, and they serve as the initial solution set of the PSO algorithm.

(4) Update the extremum. $fitness(P_g(l))$ is the global extremum of the population, $fitness(X_i(l))$ is the fitness value of the individual particle swarm, and $fitness(P_i(l-1))$ is the individual extremum value before iteration. If $fitness(X_i(l)) < fitness(P_i(l-1))$, then $P_i(l) = X_i(l)$, otherwise, $P_i(l) = P_i(l-1)$. In those expressions, l is the number of iterations. The global extremum is the individual extremum with the best fitness.

(5) Update the velocity and position. During each iteration, each particle updates its velocity and position based on its individual extremum and the global extremum. To prevent blind search, the velocity and position are constrained within specified ranges, as given by Equations (13) and (14) [41].

$$V_i(l+1) = wV_i(l) + C_1r_1(P_i(l) - X_i(l)) + C_2r_2\left(P_g(l) - X_i(l)\right) \tag{13}$$

$$X_i(l+1) = X_i(l) + V_i(l+1) \tag{14}$$

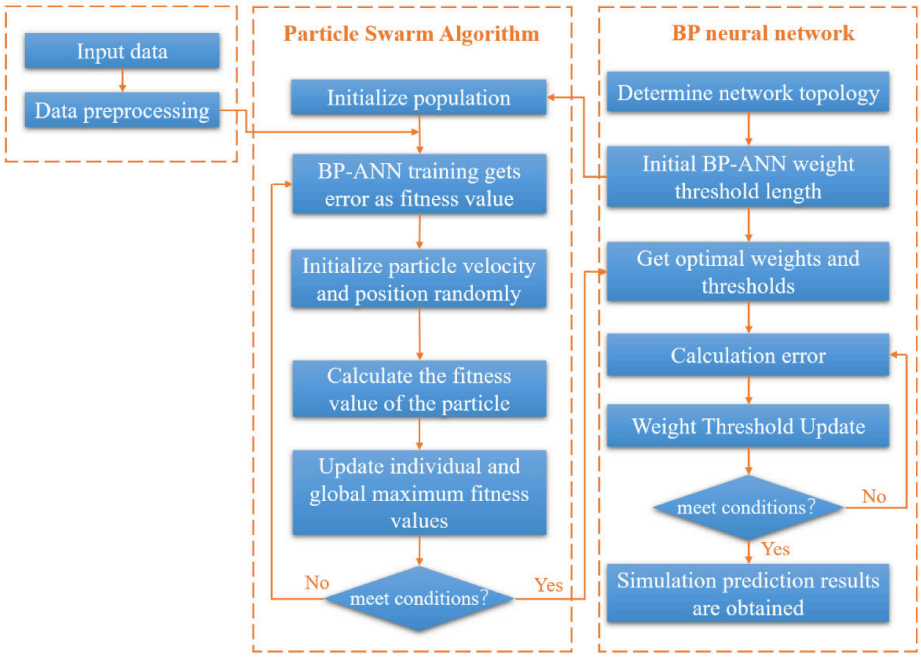


Figure 6. Basic structure of PSO-BP-ANN.

Table 7. Optimal parameters of PSO-BP-ANN model for four types of PFHEs.

Content	Straight Fin		Wavy Fin		Louver Fin		Serrated Fin	
	j	*f*	*j*	*f*	*j*	*f*	*j*	*f*
Maximum number of iterations	150	150	150	250	100	150	150	50
Population size	150	100	100	100	50	100	30	100
Acceleration factor	1.5	1.5	2.5	0.5	2/0.5	1/2.5	0.4	0.4
Inertia weight	1	1	1	1	1	1	1	1

3.3. Prediction Results and Error Analysis

3.3.1. Performance Prediction Results Based on BP-ANN Model

The trained BP-ANN model is used to predict the test set data, and the predicted values are compared with the experimental ones in the database, as shown in Figure 7. The mean absolute percentage errors (*MAPE*) of the BP-ANN model predictions for the four types of PFHEs are all within 10%, indicating an overall good predictive performance. However, some predicted values still exhibit deviations with errors exceeding 10%. Therefore, in applications where high precision is required, further optimization is still needed to improve the prediction accuracy and stability of the BP-ANN model.

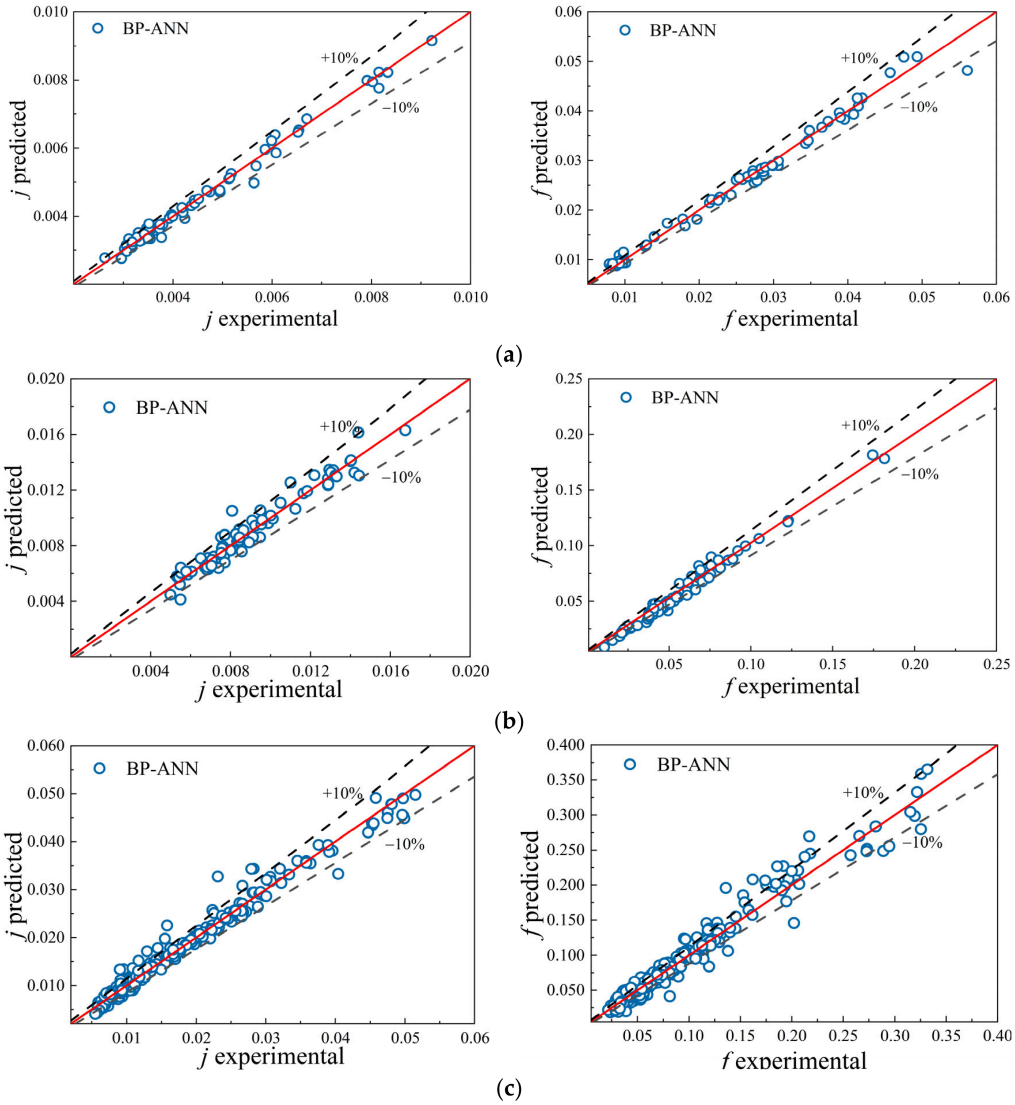
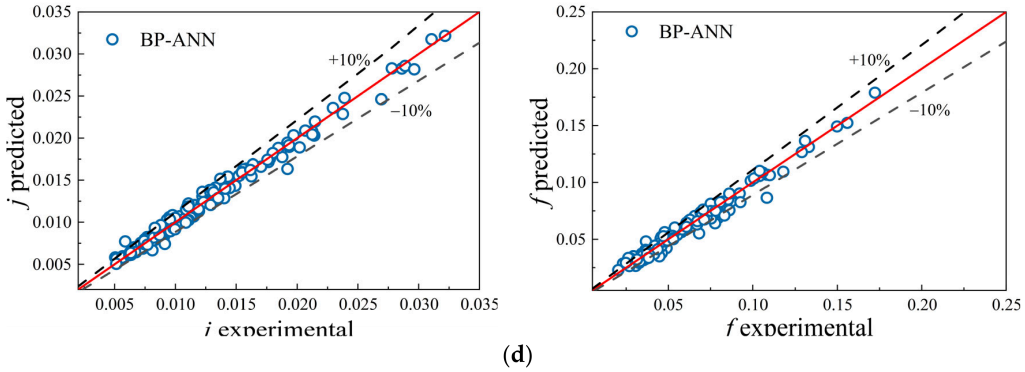


Figure 7. *Cont.*



(**d**)

Figure 7. Comparison of predicted and experimental values of the test set data for the four types of PFHEs: (**a**) straight fin; (**b**) wavy fin; (**c**) louver fin; (**d**) serrated fin. The red solid lines denote the 1:1 reference lines between predicted and experimental values, and the dashed lines denote the ±10% error bounds.

3.3.2. Performance Optimization Results Based on PSO-BP-ANN Model

The relative errors between the predictions of the PSO-BP-ANN and BP-ANN models for the four types of PFHEs are compared in Figure 8. The error for each data point was calculated as the difference between the model-predicted value and the corresponding experimental value from the database. Table 8 provides a quantitative comparison of the predictive performance of the two models for the j and f factors. The results show that, based on the selected training/test split (85% training, 15% testing) and the database used in this study, the PSO-BP-ANN model overcomes the adverse impact of random initial weights and thresholds on BP-ANN predictions, and achieves higher prediction accuracy and better stability compared with BP-ANN.

Table 8. Comparison of Simulation Results Based on BP-ANN and PSO-BP-ANN Models.

Fin Type	Neural Networks		*MAPE*	Maximum Deviation	Error More Than 10%
Straight fin	BP	j	2.5%	21.2%	3%
		f	4.35%	35.5%	18%
	PSO-BP	j	2.07%	8.4%	0%
		f	3.47%	19.7%	8.96%
Wavy fin	BP	j	5.64%	30.2%	17.5%
		f	5.63%	20.1%	13.8%
	PSO-BP	j	2.16%	9.9%	0%
		f	1.63%	10.3%	1.25%
Louver fin	BP	j	6.13%	47.6%	16.7%
		f	9.9%	47.6%	37.8%
	PSO-BP	j	4.86%	27%	12.2%
		f	8.64%	23.4%	28.8%
Serrated fin	BP	j	5.02%	31.1%	20%
		f	6.58%	30%	25%
	PSO-BP	j	4.32%	18%	11%
		f	5.24%	23.5%	17.5%

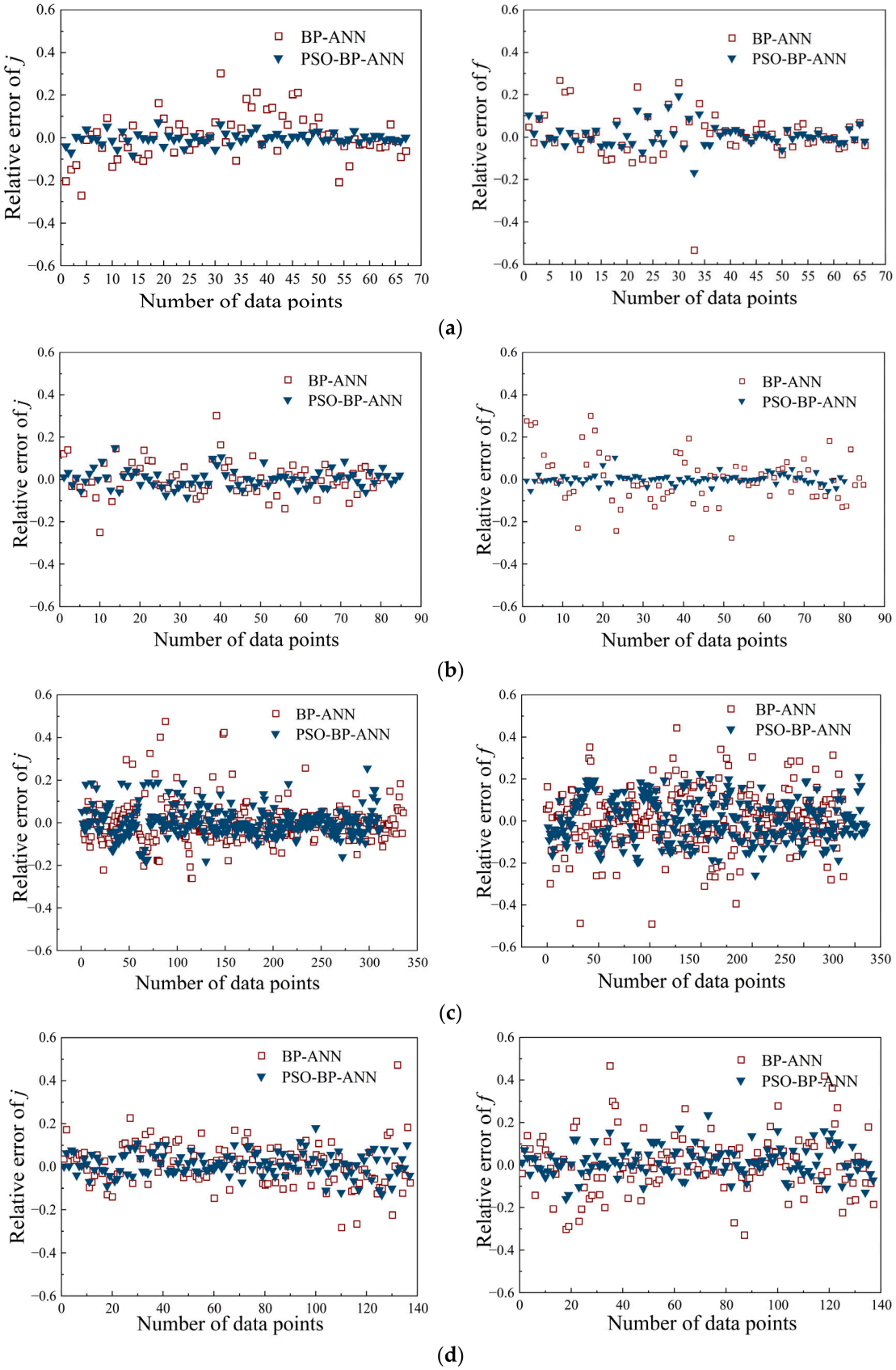


Figure 8. Relative error comparison between PSO-BP-ANN and BP-ANN results for the four types of PFHEs: (**a**) straight fin; (**b**) wavy fin; (**c**) louver fin; (**d**) serrated fin.

3.3.3. Performance Comparison Between PSO-BP-ANN and Associative Predictions

To further verify the generalization ability of the optimized model, the PSO-BP-ANN model and several empirical correlations were evaluated against independent experimental data from the channel database of the four types of PFHEs. As shown in Figure 9, the correlations yield calculated results that cover only a limited range and exhibit large errors. The main reasons are considered as follows: 1. PFHE structures involve complex parameters, and the correlations may rely on fewer dependent variables, making it difficult to accurately represent the *j* and *f* factors; 2. flow and heat transfer in the HE can be affected by temperature variations, introducing additional uncertainty; and 3. the experimental data are applicable only to limited operating conditions. By contrast, the PSO-BP-ANN model does not require any explicit relationship between input and output. Within the database and parameter ranges adopted in this study, it offers significant advantages over empirical correlations in both prediction accuracy and convenience.

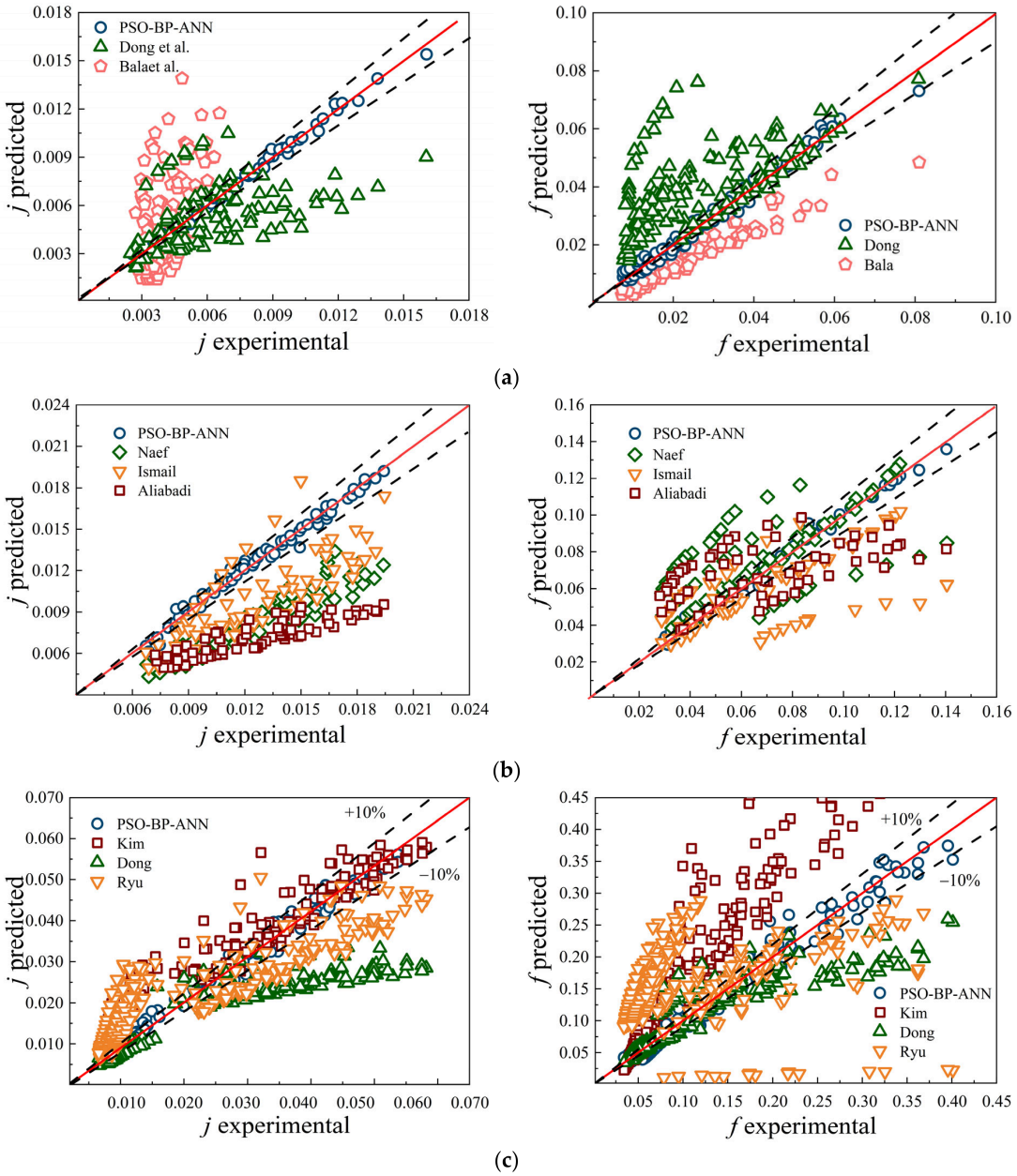


Figure 9. *Cont.*

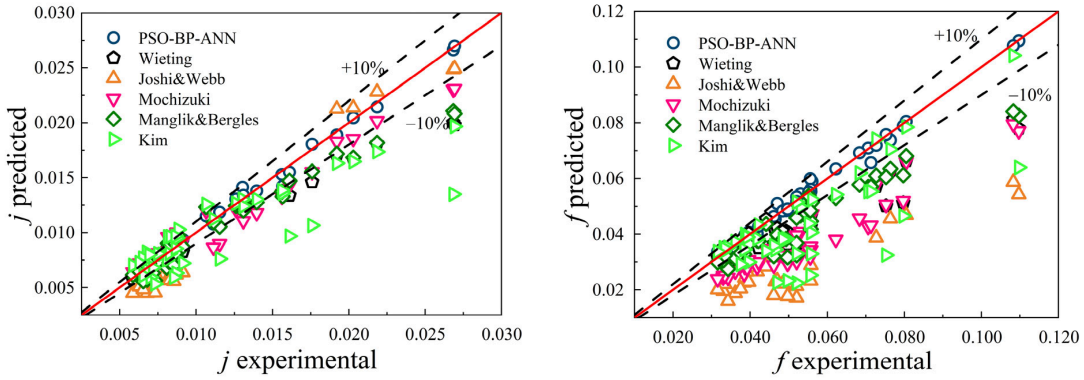


Figure 9. Comparison between PSO-BP-ANN and empirical correlation performance prediction of the four types of PFHEs: (**a**) straight fin; (**b**) wavy fin; (**c**) louver fin; (**d**) serrated fin. The red solid lines denote the 1:1 reference lines between predicted and experimental values, and the dashed lines denote the ±10% error bounds [24,27,28,33,34,38–49].

Although the PSO-BP-ANN model shows improved prediction accuracy, the database used in this study contains data from both literature sources and CFD simulations, and therefore different levels of uncertainty may exist. For the CFD data, numerical uncertainty was reduced through grid-independence verification, in which the variations in the j and f factors were less than 1%, and the CFD results were further validated against experimental data with MAPE values of 8.07% and 9.28% for j and f, respectively. For the ML predictions, the residual errors on the test set were quantified using MAPE, maximum deviation, and the proportion of samples with errors greater than 10%. Therefore, the Pareto-front solution should be regarded as a robust engineering trade-off within the investigated geometric and Re ranges, rather than a universal optimum outside the database domain.

4. Multi-Objective Optimization Strategy Analysis

4.1. Establishment of NSGA-II Optimization Method for Serrated Fin Channels

Among the numerous enhanced fin structures, serrated fins are the most widely used. This type of fin is recognized as having high surface density, strong reliability, and significantly enhanced heat transfer due to boundary layer disruption and reattachment in interrupted channels. Nonetheless, it is prone to large pressure drops, resulting in high operating costs. Therefore, it is necessary to find a trade-off between enhanced heat transfer and increased pressure drop in serrated fin PFHEs. In this section, the PSO-BP-ANN model for the serrated fin channel was coupled with NSGA-II to search for a set of non-dominated solutions. The optimization was carried out at Re = 800. The objective functions were defined as maximizing the heat transfer factor j and minimizing the friction factor f. The design variables were the fin height F_h, fin spacing F_p, fin thickness t, and fin length L_d, with the following bounds: $2.7 \le F_h \le 9.3$ mm, $1.2 \le F_p \le 3.2$ mm, $0.1 \le t \le 0.5$ mm, and $3 \le L_d \le 9$ mm. These bounds were consistent with the structural range used to construct the serrated fin database. The optimization design of the HE is performed subject to the constraints given in Equation (15). The entire optimization process is shown in Figure 10. By combining the PSO-BP-ANN prediction model with NSGA-II, the structural parameters of the Z-shaped channel PFHE are optimized, and a Pareto optimal solution set is obtained. The operating parameters of NSGA-II are shown in Table 9.

$$\begin{aligned} \text{Objectives}: & \begin{cases} \text{Maximize}: j = net_j\left(F_p/F_h, t/F_p, t/L_d, Re\right) \\ \text{Minimize}: \ f = net_f\left(F_p/F_h, t/F_p, t/L_d, Re\right) \end{cases} \\ \text{Design variables}: & 2.7 \le F_h \le 9.3; 1.2 \le F_p \le 3.2; 0.1 \le t \le 0.5; 3 \le L_d \le 9; (\text{mm}) \end{aligned} \quad (15)$$

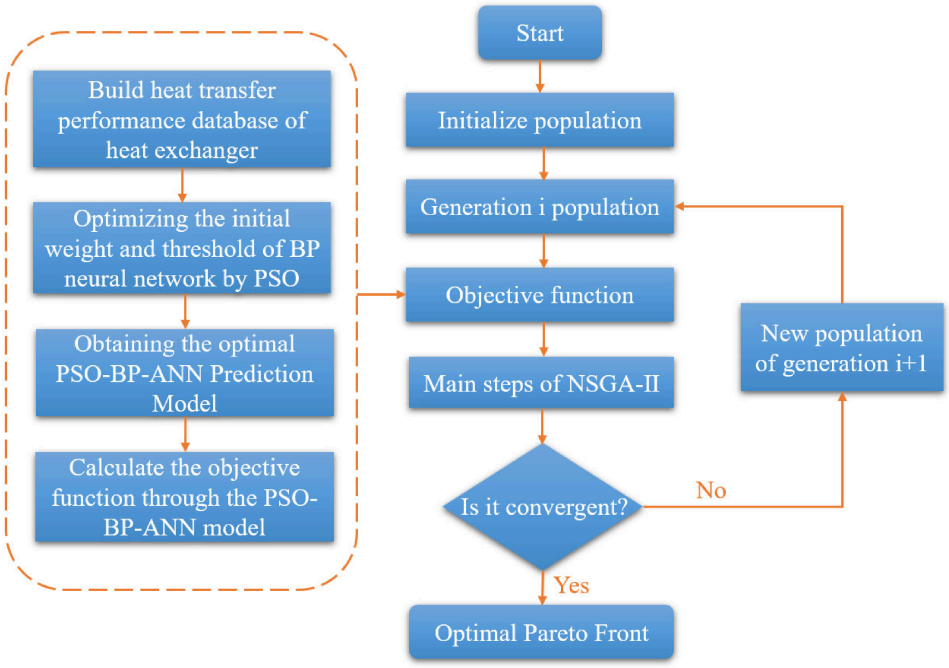


Figure 10. Flow chart of the optimization process.

Table 9. Parameter settings of the NSGA-II.

Parameter	Value
Population size	250
Iterations	200
Pareto score	0.3
Functional Tolerance	10^{-4}

With NSGA-II, after 250 generations of evolution, a set of Pareto optimal points for the serrated fin channel is obtained at Re = 800. The optimization goal is to minimize the f factor while maintaining the same j factor, as shown in Figure 11. Each point in this figure contains comprehensive information on the two objective functions and the four structural parameters.

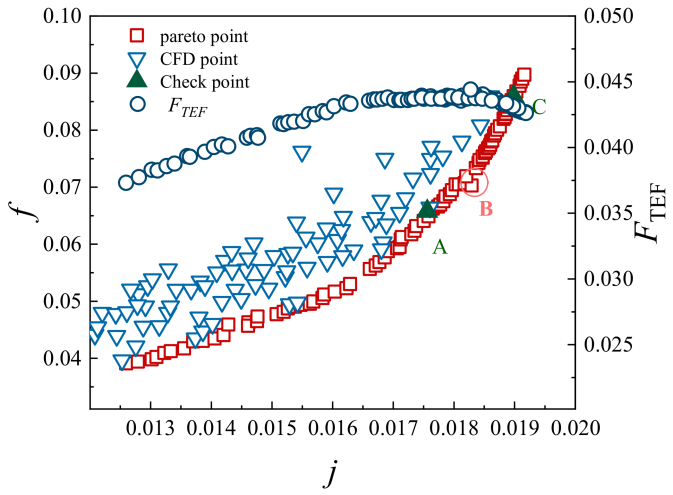


Figure 11. Pareto optimization results. Points A, B, and C denote three representative Pareto optimal solutions selected for further parameter analysis, and the circles indicate the F_{TEF} values.

In Figure 11, the open triangles represent some of the CFD numerical results from the single-factor analysis of the serrated fin channel. The open rectangles represent the Pareto optimal solution set obtained using the predicted values of the PSO-BP-ANN model. As can be seen, the Pareto front rises monotonically at first and then gradually becomes steeper toward the end. After the j factor reaches 0.019, the Pareto curve shows that the distribution of points rises almost vertically. The curve indicates that the j factor of the HE is positively correlated with the f factor. This suggests that simply pursuing higher heat transfer performance or minimum flow resistance alone often cannot yield HE products that meet engineering requirements.

Based on the Pareto curve in Figure 11, three points (A, B, and C) are selected for further parameter analysis. Mathematically, A, B, and C are all Pareto optimal solutions. Compared with the original design, all three points exhibit varying degrees of improvement in heat transfer performance. Relative to point A, the f factor at point B increases by 7.33%, while the j factor increases by 8.09%. Compared with point B, point C increases the j factor by only 3.71%, but the f factor increases by 21.74%. Beyond point C, further enhancement of heat transfer performance through changes in structural parameters alone becomes extremely limited.

The F_{TEF} shown in Figure 11 is used to evaluate the comprehensive heat transfer performance of the Pareto point set. As can be seen, point B exhibits the best flow and heat transfer performance. The Pareto optimization results at point B are compared with the numerical simulation results in Table 10. The relative errors for the j factor, f factor, and F_{TEF} are 4%, 4.9%, and 2.2%, respectively. Therefore, selecting the parameter combination at point B as the optimum is reasonable.

Table 10. Numerical verification result of point B.

	F_h/mm	F_p/mm	t/mm	L_d/mm	j	f	F_{TEF}
Optimal Solution B	9.29	1.22	0.16	3.06	0.0183	0.0706	0.0442
CFD verification					0.0176	0.0673	0.0433
Relative error/%					4.0	4.9	2.2

4.2. Analysis of Optimization Results

Figure 12 shows the CFD simulation results for the inlet working fluid at Re = 800 and the influences of fin height (F_h), fin pitch (F_p), fin thickness (t), and fin length (L_d) on the flow and heat transfer of the serrated fin HE. The variation in these parameters gives a physical explanation for the Pareto solution. Increasing F_h enlarges the fin surface exposed to the air stream and strengthens the interaction between the flow and the wall, so the heat transfer factor and the comprehensive performance tend to increase when the pressure drop is allowable. A smaller F_p narrows the flow passage and enhances the near-wall velocity gradient, which improves heat transfer but also increases flow resistance. A shorter L_d interrupts the boundary layer more frequently and promotes its redevelopment along the fin surface; however, this also produces an additional pressure-drop penalty. The effect of t is more sensitive to flow resistance. As t increases, both j and f increase, while reducing t can decrease f with only a limited change in j. Therefore, a smaller fin thickness is more suitable for low-pressure design. Furthermore, j and f exhibit different correlations with the four structural parameters, which is consistent with the correlation analysis results in Figure 13. The flow and heat transfer performance is further evaluated using the comprehensive heat transfer factor, F_{TEF}, expressed in Equation (16) [50]. When the values of F_h, F_p, t, and L_d are 9.29, 1.22, 0.16, and 3.06, respectively, the flow and heat transfer performance reaches its optimum, which is also consistent with the Pareto optimal

solution (Figure 11). This further demonstrates the high accuracy of the multi-objective optimization method combining CFD, PSO-BP-ANN, and NSGA-II.

$$F_{TEF} = j/f^{1/3} \tag{16}$$

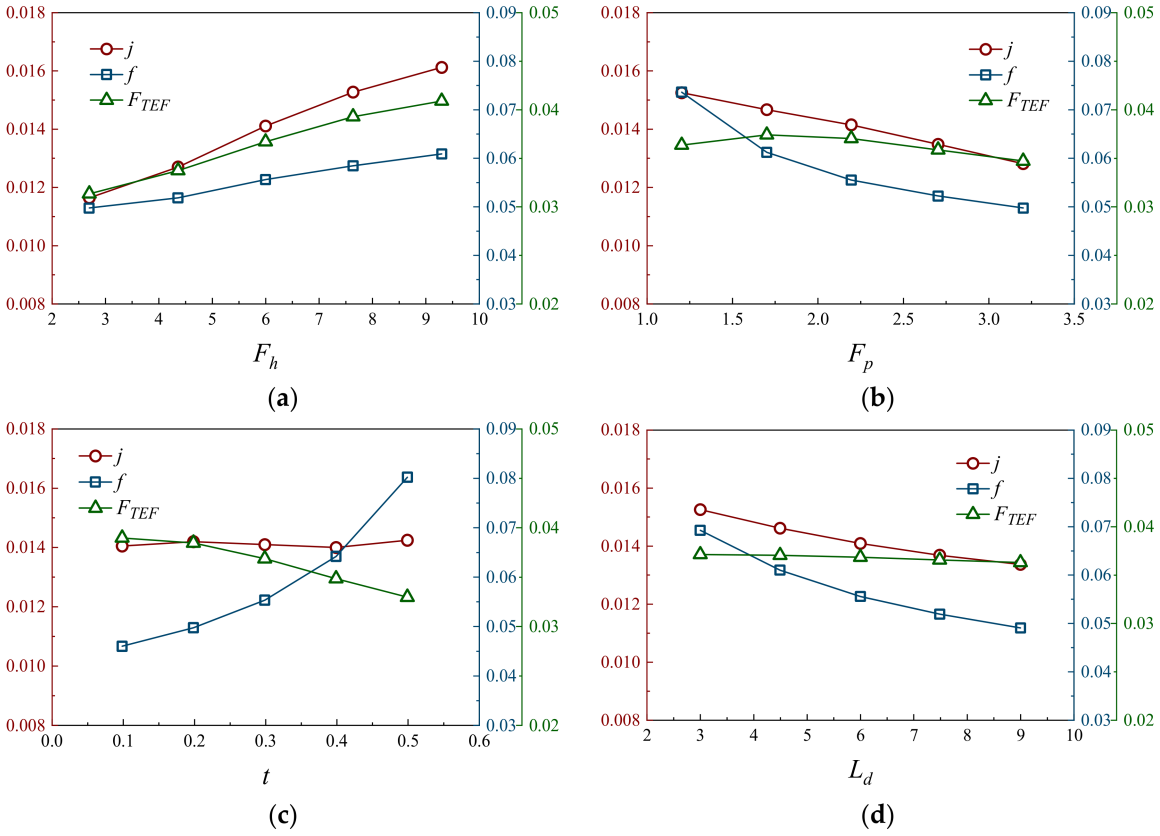


Figure 12. Influence of single fin parameters on heat transfer characteristics: (**a**) fin height; (**b**) fin spacing; (**c**) fin thickness; (**d**) fin length.

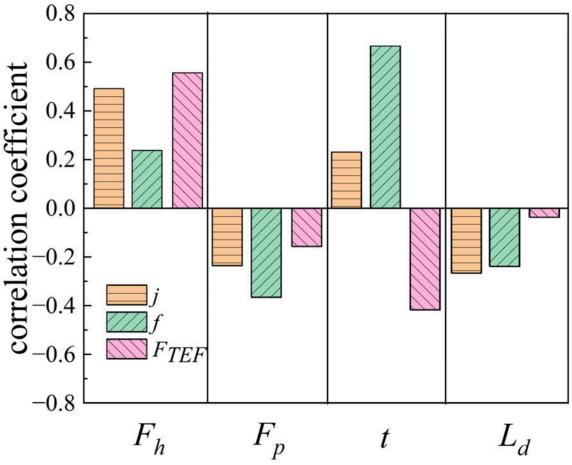
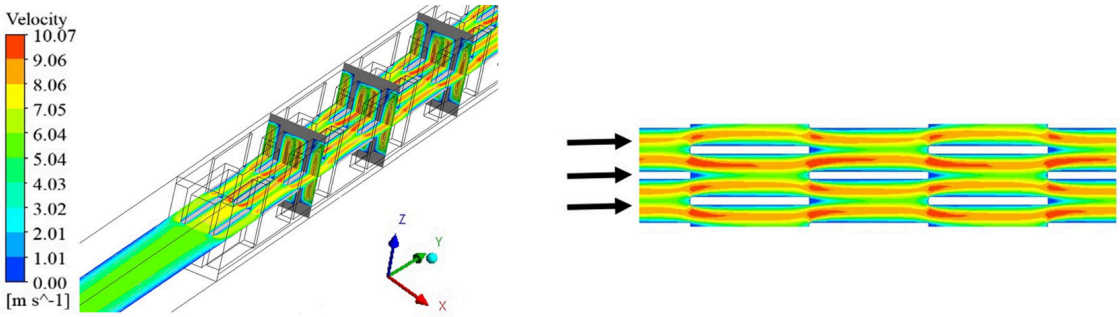


Figure 13. Correlation of structural parameters.

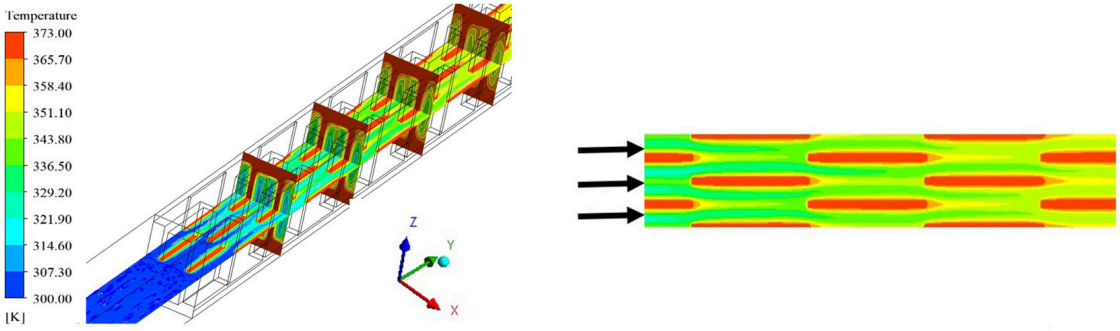
Figures 14 and 15 further support this interpretation. The reduction in the flow cross-sectional area increases the velocity in the main flow region. When the air flows through each fin unit, it is redistributed near the fin leading edge, with a lower velocity at the front of the fin and higher velocities on both sides. The temperature field follows a similar development pattern. A thermal boundary layer forms on the fin surface and is

then periodically destroyed and redeveloped. Therefore, the optimized geometry is not simply the structure with the largest j factor. It represents a balance between boundary-layer renewal, available fin surface, and flow-resistance penalty. The F_{TEF} comparison in Figure 14, and the CFD verification in Table 10 also show that the selected parameter combination is consistent with the thermal–hydraulic trade-off of the serrated fin channel.



(**a**) (**b**)

Figure 14. Velocity distribution of each section: (**a**) X-Z section and X-Y section, (**b**) partial enlargement of X-Y section. The arrows indicate the flow direction.



(**a**) (**b**)

Figure 15. Temperature distribution of each section: (**a**) X-Z section and X-Y section, (**b**) partial enlargement of X-Y section. The arrows indicate the flow direction.

5. Conclusions

This paper employs a multi-objective optimization method combining CFD, PSO-BP-ANN, and NSGA-II to predict and optimize the performance of four types of PFHE channels. The main conclusions are as follows:

(1) Based on the heat transfer and resistance databases of four types of PFHE channels established by the CFD simulation and empirical correlations, through training, the PSO-BP-ANN prediction model compared to the BP-ANN model, has higher prediction accuracy and generalization ability.

(2) The comparison between the PSO-BP-ANN model predictions and the empirical correlations on independent experimental data proves that the ANN can effectively replace those correlations in predicting the thermal and hydraulic characteristics of PFHEs. The PSO-BP-ANN model shows a wider applicable range and higher accuracy.

(3) Based on the predictions of the PSO-BP-ANN model for serrated fin channels, NSGA-II was used to optimize the structural variables (F_h, F_p, t, L_d) with respect to the two objective functions (j and f). The results show that, under laminar flow conditions (Re = 800), the serrated fin HE achieves the best heat transfer performance when the fin height, spacing, thickness, and length are 9.29, 1.22, 0.16, and 3.06, respectively.

Author Contributions: Conceptualization, X.D. and L.G.; methodology, X.D.; software, Z.H.; validation, Y.Z.; formal analysis, Z.H.; investigation, Z.H.; resources, L.G. and X.D.; data curation, C.Z.; writing—original draft preparation, Y.Z.; writing—review and editing, Y.Z. and L.L.; visualization, Z.H.; supervision, C.Z.; project administration, X.D.; funding acquisition, X.D. All authors have read and agreed to the published version of the manuscript.

Funding: This research was funded by the National Natural Science Foundation of China (No. U224120437, No. 52276090).

Data Availability Statement: The data presented in this study are available on request from the corresponding author. The data are not publicly available due to confidentiality restrictions associated with the experimental measurements, simulation models, and ongoing research project.

Conflicts of Interest: The authors declare no conflicts of interest.

Appendix A

Appendix A.1. Performance Database for Straight Fin Channels

The main geometric parameters of straight fin channels are fin spacing F_p, fin height F_h, fin thickness t, and channel length L_d. A database containing 880 performance data points was established through a literature survey; the corresponding fin structural parameters are listed in Table A1. Among them, the experimental data of Kays and London [23] are the most influential, covering straight fin channels with $L_d > 65$ mm and $L_d/D_e > 20$ (where D_e is the hydraulic diameter). Dong et al. [24] experimentally investigated straight fin channels with $L_d < 65$ mm and $L_d/D_e < 20$, effectively supplementing the data of Kays and London.

Table A1. Structural parameters of straight fins in the database.

Reference	Surfaces	*Re*	F_p/mm	F_h/mm	t/mm	L_d/mm	D_e/mm
Kays and London [23]	1	4000–60,000	12.70	19.05	0.813	304.8	14.45
	2	3000–45,000	8.44	19.05	0.813	304.8	10.82
	3	2500–35,000	6.40	19.05	0.813	304.8	8.59
	4	600–10,000	4.79	11.94	0.152	63.2	6.15
	5	800–12,000	4.10	10.29	0.254	30.5	5.54
	6	800–15,000	2.81	20.9	0.203	30.2	4.64
	7	500–10,000	2.29	6.35	0.152	63.5	3.08
	8	500–10,000	2.29	12.19	0.203	203.2	3.52
	9	500–10,000	1.72	8.38	0.152	63.8	2.59
	10	500–6000	1.68	10.62	0.152	173.7	2.67
	11	400–8000	1.28	6.35	0.152	63.8	1.875
	12	400–10,000	2.47	13.82	0.254	127	3.84
	13	300–10,000	2.13	6.33	0.152	127	2.86
	14	200–8000	2.12	6.35	0.152	63.5	2.87
	15	300–5000	1.50	6.5	0.152	127	1.722
	16	300–3000	0.98	5.18	0.152	63.5	1.151
	17	300–3000	0.84	8.76	0.152	63.5	1.222
	18	500–2000	0.55	2.54	0.051	66.8	0.805
Dong et al. [24]	19	600–7000	4	8	0.2	65	4.391
	20	600–7000	4.5	8	0.2	65	4.727
	21	600–7000	5	8	0.2	65	5.02
	22	600–7000	4	8	0.2	53	4.391
	23	600–7000	4	7	0.15	43	4.242
	24	600–7000	4	8	0.15	43	4.53
	25	600–7000	4	10	0.15	43	4.979
	26	600–7000	4	8	0.2	55	4.391
	28	600–7000	5	8	0.2	55	5.02
	29	600–7000	4	7	0.15	41	4.242

Table A1. *Cont.*

Reference	Surfaces	*Re*	F_p/mm	F_h/mm	t/mm	L_d/mm	D_e/mm
Dong et al. [24]	27	600–7000	4.5	8	0.2	55	4.727
	30	600–7000	4.5	7	0.15	41	4.524
	31	600–7000	5	7	0.15	41	4.767
	32	600–7000	4	8	0.15	41	4.53
	33	600–7000	4	10	0.15	41	4.979

Appendix A.2. Performance Database for Wavy Fin Channels

The main geometric parameters of wavy fin channels are fin spacing F_p, fin height F_h, channel length L_d, fin thickness t, double amplitude $2A$, and wavelength L. A database containing 1056 performance data points was established through a literature survey; the corresponding fin structural parameters are listed in Table A2. The earliest experimental data on wavy fin channels were reported in the classic reference book by Kays and London [23], including three wavy fin channels. Subsequently, Gough and Shemmeri [25] presented performance data for three wavy fin channels similar to those in Kays and London based on wind tunnel experiments. Aliabadi et al. [27] obtained performance data for 15 fin channels through numerical simulation. Dong et al. [24] provided experimental performance data for 11 wavy fin channels within a *Re* range of 800–6500. Naef et al. [28] computed the performance data for 21 fin channels with new geometries by numerical simulation.

Table A2. Structural parameters of wavy fins in the database.

Reference	Surfaces	*Re*	F_p/mm	F_h/mm	L_d/mm	t/mm	$2A$/mm	L/mm
Kays and London [23]	1	500–8000	2.22	10.49	52.5	0.152	1.97	9.53
	2	400–10,000	2.21	9.53	52.5	0.254	1.98	9.53
	3	600–5000	1.43	10.49	52.5	0.152	1.97	9.53
Gough and Shemmeri [25]	4	300–4000	2.44	8.59	52.5	0.16	1.47	9.6
	5	300–3000	1.50	7.95	52.5	0.16	1.5	7.5
	6	500–5000	2.78	10.0	52.8	0.16	2.78	11.5
Dong et al. [24]	7	690–6200	2.0	8.0	65.0	0.20	1.5	10.8
	8	750–6800	2.25	8.0	65.0	0.20	1.5	10.8
	9	800–7300	2.5	8.0	65.0	0.20	1.5	10.8
	10	750–6750	2.0	8.0	53.0	0.20	1.5	10.8
	11	600–6000	2.25	8.0	53.0	0.20	1.5	10.8
	12	600–6000	2.5	8.0	53.0	0.20	1.5	10.8
	13	700–6400	2.0	7.0	43.0	0.20	1.5	10.8
	14	600–6000	2.25	7.0	43.0	0.20	1.5	10.8
	15	600–6000	2.5	7.0	43.0	0.20	1.5	10.8
	16	700–6200	2.0	8.0	43.0	0.20	1.5	10.8
	17	670–6300	2.0	10.0	43.0	0.20	1.5	10.8
Aliabadi et al. [27]	18	710–6400	2.0	7.0	43.0	0.30	1.5	10.8
	19	690–6400	2.0	7.0	43.0	0.10	1.5	10.8
	20	600–6000	0.2	8.0	65.0	0.20	2.0	10.8
	21	600–6000	0.2	8.0	65.0	0.20	1.0	10.8
Naef et al. [28]	22	1100–11,500	5.0	5.0	30.0	0.20	0.3	15.0
	23	1150–11,500	5.0	5.0	30.0	0.20	5.0	15.0
	24	1000–11,000	5.0	5.0	30.0	0.20	6.0	15.0
	25	1000–10,100	5.5	4.0	30.0	0.05	2.0	15.0
	26	970–9800	6.0	4.0	20.0	0.05	0.6	5.0

Table A2. *Cont.*

Reference	Surfaces	*Re*	F_p/mm	F_h/mm	L_d/mm	t/mm	2A/mm	L/mm
Naef et al. [28]	27	1100–10,600	6.5	4.0	20.0	0.20	0.6	5.0
	28	1000–10,100	5.5	4.0	30.0	0.05	0.6	15.0
	29	1050–10,300	6.0	4.0	30.0	0.20	0.6	15.0
	30	1000–10,100	6.5	4.0	30.0	0.05	0.6	15.0
	31	1050–10,300	5.5	4.0	30.0	0.20	0.6	15.0
	32	970–9800	6.0	4.0	30.0	0.05	0.6	15.0
	33	1000–10,100	6.5	4.0	30.0	0.05	0.6	15.0
	34	1000–10,200	5.0	5.0	20.0	0.05	0.6	5.0
	35	1000–10,200	5.0	5.0	30.0	0.05	0.6	15.0
	36	1100–10,900	5.5	4.0	30.0	0.45	0.6	15.0
	37	950–9500	5.5	4.0	30.0	0.45	0.4	15.0
	38	1050–10,600	5.0	5.0	30.0	0.45	0.6	15.0
	39	1050–10,700	6.0	4.0	20.0	0.45	0.6	5.0
	40	1000–10,100	5.5	4.0	20.0	0.05	0.6	5.0
	41	1000–10,400	6.0	4.0	20.0	0.2	0.6	5.0
	42	1000–11,000	6.5	4.0	20.0	0.05	0.6	5.0

Appendix A.3. Performance Database for Louver Fin Channels

The main geometric parameters of louver fin channels are fin spacing F_p, fin height F_h, channel length L_d, fin thickness t, louver angle L_a, and louver pitch L_p. A database containing 4166 performance data points was established through a literature survey; the corresponding fin structural parameters are listed in Table A3. Chang and Wang [29–32] compiled 91 performance data points for louver fin channels. Kim et al. [33] obtained 45 performance data points through experimental investigation. Dong et al. [34] obtained 20 performance data points experimentally.

Table A3. Structural parameters of louvered fins in the database.

Reference	Surfaces	*Re*	F_p/mm	F_h/mm	L_d/mm	t/mm	L_a/°	L_p/mm
Chang and Wang [29–32]	1	100–3000	1.55	12.7	40	0.075	8.43	3
	2	100–3000	1.55	12.7	40	0.075	10.37	3
	3	100–3000	1.6	12.7	40	0.075	16.66	3
	4	100–3000	1.55	12.7	40	0.075	13.36	2.25
	5	100–3000	1.56	12.7	40	0.075	16	2.25
	6	100–3000	1.56	12.7	40	0.075	19.2	2.25
	7	100–3000	1.55	12.7	40	0.075	18.8	1.8
	8	100–3000	1.585	12.7	40	0.075	20.83	1.8
	9	100–3000	1.575	12.7	40	0.075	27.82	1.8
	10	100–3000	1.525	12.7	40	0.075	19.63	1.5
	11	100–3000	1.625	12.7	40	0.075	14.15	1.8
	12	100–3000	1.56	12.7	40	0.075	11.15	3
	13	100–3000	1.675	12.7	40	0.075	24.14	2.25
	14	100–3000	1.65	12.7	40	0.075	21.37	2.25
	15	100–3000	1.65	12.7	40	0.075	21.37	2.25
	16	100–3000	1.625	12.7	40	0.075	21.37	2.25
	17	100–3000	1.6	12.7	40	0.075	20.28	2.25
	18	100–3000	1.535	7.8	40	0.075	13.89	3
	19	100–3000	1.525	7.8	40	0.075	13.78	2.25
	20	100–3000	1.535	7.8	40	0.075	20.42	1.8
	21	100–3000	1.55	7.8	40	0.075	26.1	1.5
	22	100–3000	1.485	7.8	40	0.075	9.52	2.25
	23	100–3000	1.51	7.8	40	0.075	16.53	2.25

Table A3. *Cont.*

Reference	Surfaces	*Re*	F_p/mm	F_h/mm	L_d/mm	t/mm	L_a/°	L_p/mm
Chang and Wang [29–32]	24	100–3000	1.51	7.8	40	0.075	17.7	2.25
	25	100–3000	1.225	7.8	40	0.075	16	2.25
	26	100–3000	1.005	7.8	40	0.075	13.89	2.25
	27	100–3000	1.535	7.8	40	0.075	14.15	2.25
	28	100–3000	1.51	7.8	40	0.075	16.63	2.25
	29	100–3000	1.535	7.8	40	0.075	17.59	2.25
	30	100–3000	1.5	7.8	40	0.075	14.41	2.25
	31	100–3000	1.8	16	22	0.16	28	1.318
	32	100–3000	2	16	22	0.16	28	1.318
	33	100–3000	2.2	16	22	0.16	28	1.318
	34	100–3000	1.8	19	22	0.16	28	1.42
	35	100–3000	2	19	22	0.16	28	1.42
	36	100–3000	2.2	19	22	0.16	28	1.42
	37	100–3000	1.8	16	26	0.16	28	1.481
	38	100–3000	2	16	26	0.16	28	1.481
	39	100–3000	2.2	16	26	0.16	28	1.481
	40	100–3000	1.8	19	26	0.16	28	1.534
	41	100–3000	2	19	26	0.16	28	1.534
	42	100–3000	2.2	19	26	0.16	28	1.534
	43	100–3000	1.8	16	32	0.16	28	1.693
	44	100–3000	2	16	32	0.16	28	1.693
	45	100–3000	2.2	16	32	0.16	28	1.693
	46	100–3000	1.8	19	32	0.16	28	1.546
	47	100–3000	2	19	32	0.16	28	1.546
	48	100–3000	2.2	19	32	0.16	28	1.546
	49	100–3000	1.8	19	38	0.16	28	1.86
	50	100–3000	2	19	38	0.16	28	1.86
	51	100–3000	2.2	19	38	0.16	28	1.86
	52	100–3000	1.8	16	44	0.16	28	1.59
	53	100–3000	2	16	44	0.16	28	1.59
	54	100–3000	2.2	16	44	0.16	28	1.59
	55	100–3000	1.8	19	44	0.16	28	1.532
	56	100–3000	2	19	44	0.16	28	1.532
	57	100–3000	2.2	19	44	0.16	28	1.532
	58	100–3000	1.124	8	16	0.157	30	1
	59	100–3000	1.954	9.22	20.32	0.0508	27	1.016
	60	100–3000	1.588	9.22	20.32	0.0508	27	1.016
	61	100–3000	1.27	9.22	20.32	0.0508	27	1.016
	62	100–3000	1.114	9.15	16.26	0.127	27	0.94
	63	100–3000	2.02	9	41.6	0.05	25.5	1.4
	64	100–3000	3.25	9	41.6	0.05	25.5	1.4
	65	100–3000	1.65	9	41.6	0.05	25.5	1.4
	66	100–3000	2.09	9	41.6	0.05	21.5	1.4
	67	100–3000	2.03	9	41.6	0.05	28.5	1.4
	68	100–3000	2.15	9	20.8	0.05	25.5	1.4
	69	100–3000	1.7	9	20.8	0.05	25.5	1.4
	70	100–3000	2.11	9	41.6	0.05	29	0.81
	71	100–3000	1.72	9	41.6	0.05	29	0.81
	72	100–3000	3.33	9	41.6	0.05	29	0.81
	73	100–3000	2.18	9	41.6	0.05	30	1.1
	74	100–3000	2.16	9	41.6	0.05	20	0.81
	75	100–3000	2.16	6	41.6	0.05	28	1.1
	76	100–3000	2.17	12	41.6	0.05	22	1.1
	77	100–3000	2.17	6	41.6	0.05	22	1.1
	78	100–3000	2.117	18.923	25.4	0.1575	30	1.397
	79	100–3000	1.693	18.923	25.4	0.1575	30	1.397
	80	100–3000	1.411	18.923	25.4	0.1575	30	1.397

Table A3. *Cont.*

Reference	Surfaces	*Re*	F_p/mm	F_h/mm	L_d/mm	t/mm	L_a/°	L_p/mm
Chang and Wang [29–32]	81	100–3000	2.117	8.64	25.4	0.1575	30	1.65
	82	100–3000	1.693	8.64	25.4	0.1575	30	1.65
	83	100–3000	1.411	8.64	25.4	0.1575	30	1.65
	84	100–3000	0.51	2.84	15.6	0.0254	25	0.85
	85	100–3000	1	12.5	57.4	0.06	22	1.4
	86	100–3000	2	12.4	57.4	0.06	18.5	1.4
	87	100–3000	2	12.4	37	0.06	24.5	1.3
	88	100–3000	1.8	8.6	37	0.04	24	1.2
	89	100–3000	1.8	9.6	50	0.06	25.5	1.1
	90	100–3000	1.9	8	47.8	0.04	28.5	0.5
	91	100–3000	1.5	20	50	0.16	35	1.884
Kim et al. [33]	92	100–600	1.4	8.15	16	0.1	23	1.7
	93	100–600	1.4	8.15	16	0.1	25	1.7
	94	100–600	1.4	8.15	16	0.1	27	1.7
	95	100–600	1.4	8.15	16	0.1	29	1.7
	96	100–600	1.4	8.15	20	0.1	15	1.7
	97	100–600	1.4	8.15	20	0.1	17	1.7
	98	100–600	1.4	8.15	20	0.1	19	1.7
	99	100–600	1.4	8.15	20	0.1	21	1.7
	100	100–600	1.4	8.15	20	0.1	23	1.7
	101	100–600	1.4	8.15	20	0.1	25	1.7
	102	100–600	1.4	8.15	20	0.1	27	1.7
	103	100–600	1.4	8.15	24	0.1	23	1.7
	104	100–600	1.4	8.15	24	0.1	25	1.7
	105	100–600	1.4	8.15	24	0.1	27	1.7
	106	100–600	1.4	8.15	24	0.1	29	1.7
	107	100–600	1	8.15	16	0.1	23	1.7
	108	100–600	1	8.15	20	0.1	23	1.7
	109	100–600	1	8.15	24	0.1	23	1.7
	110	100–600	1.2	8.15	16	0.1	23	1.7
	111	100–600	1.2	8.15	20	0.1	23	1.7
	112	100–600	1.2	8.15	24	0.1	23	1.7
	113	100–600	1.4	8.15	16	0.1	23	1.7
	114	100–600	1.4	8.15	20	0.1	23	1.7
	115	100–600	1.4	8.15	24	0.1	23	1.7
Dong et al. [34]	116	200–2500	2	8	65	0.2	28	1.2
	117	200–2500	2.25	8	65	0.2	28	1.2
	118	200–2500	2.5	8	65	0.2	28	1.2
	119	200–2500	2	8	53	0.2	28	1.2
	120	200–2500	2.25	8	53	0.2	28	1.2
	121	200–2500	2.5	8	53	0.2	28	1.2
	122	200–2500	2	7	36.6	0.2	28	1.2
	123	200–2500	2.25	7	36.6	0.2	28	1.2
	124	200–2500	2.5	7	36.6	0.2	28	1.2
	125	200–2500	2	10	36.6	0.2	28	1.2
	126	200–2500	2	8	36.6	0.2	28	1.2
	127	200–2500	2	8.9	65	0.15	22	1.2
	128	200–2500	2	8.9	53	0.15	22	1.2
	129	200–2500	2	8.9	36.6	0.15	22	1.2
	130	200–2500	2.25	8.9	53	0.15	22	1.2
	131	200–2500	2.5	8.9	53	0.15	22	1.2
	132	200–2500	2.75	8.9	53	0.15	22	1.2
	133	200–2500	2.25	8.9	65	0.15	22	1.2
	134	200–2500	2.5	8.9	65	0.15	22	1.2
	135	200–2500	2.75	8.9	65	0.15	22	1.2

Appendix A.4. Performance Database for Serrated Fin Channels

The main geometric parameters of serrated fin channels are fin length L_d, fin height F_h, fin pitch F_p, and fin thickness t. The fin offset is typically uniform, equal to half the fin pitch. A database containing 1840 performance data points was established through a literature survey; the corresponding dimensionless structural parameters of the fins are listed in Table A4, where $\alpha = F_p/F_h$, $\delta = t/L_d$, and $\gamma = t/F_p$. Kays and London [23] obtained 18 performance data points for serrated fin channels experimentally. Peng and Ling [35] obtained 5 performance data points experimentally.

Table A4. Dimensionless structural parameters of serrated fins in the database.

Reference	Surfaces	*Re*	α	δ	γ
Kays and London [23]	1	300–7000	0.244	0.067	0.032
	2	300–5000	0.494	0.086	0.032
	3	300–5000	0.135	0.100	0.036
	4	500–4000	0.184	0.111	0.036
	5	300–3000	0.528	0.107	0.036
	6	500–4000	0.134	0.121	0.040
	7	300–4000	0.672	0.084	0.040
	8	300–3000	0.997	0.041	0.020
	9	500–10,000	0.162	0.051	0.043
	10	300–9000	0.711	0.077	0.012
	11	200–9000	0.461	0.051	0.022
	12	500–7000	0.410	0.067	0.028
	13	500–5000	0.477	0.106	0.048
	14	500–4000	0.484	0.086	0.032
	15	500–4000	0.491	0.087	0.032
	16	300–1500	0.592	0.096	0.048
	17	300–5000	0.592	0.096	0.048
	18	400–8000	0.186	0.140	0.078
Dong et al. [34]	19	500–7500	0.231	0.111	0.040
Peng and Ling [35]	25	600–7000	0.247	0.087	0.040
	26	600–7000	0.355	0.136	0.060
	27	600–7000	0.274	0.176	0.060
	28	600–7000	0.500	0.136	0.060
	29	600–7000	0.386	0.176	0.060

References

1. Abbas, A.S.; Mohammed, A.A. Enhancement of plate-fin heat exchanger performance with aid of various types of fin configurations: A review. *J. Adv. Res. Fluid Mech. Therm. Sci.* **2022**, *99*, 48–66. [CrossRef]
2. Ozturk, M.M.; Doğan, B.; Erbay, L.B. Thermo-hydraulic performance assessment of a compact heat exchanger by varying plate fins. In *2017 IEEE 6th International Conference on Renewable Energy Research and Applications (ICRERA)*; IEEE: Piscataway, NJ, USA, 2017; pp. 70–75.
3. Turk, C.; Aradag, S.; Kakac, S. Experimental analysis of a mixed-plate gasketed plate heat exchanger and artificial neural net estimations of the performance as an alternative to classical correlations. *Int. J. Therm. Sci.* **2016**, *109*, 263–269. [CrossRef]
4. Kedam, N.; Uglanov, D.A.; Blagin, E.V.; Gorshkalev, A.A.; Panshin, R.A.; Liu, J. Unified ANN model for heat transfer factor (j) and friction factor (f) prediction in offset strip and wavy fin PFHEs. *Case Stud. Therm. Eng.* **2024**, *53*, 103845. [CrossRef]
5. Shi, H.; Chang, H.; Ma, T.; Wang, Q. Prediction of Equivalent Thermal Conduction Resistance of Printed Circuit Heat Exchangers. *J. Therm. Sci.* **2022**, *31*, 2281–2292. [CrossRef]
6. Hughes, M.T.; Kini, G.; Garimella, S. Status, challenges, and potential for machine learning in understanding and applying heat transfer phenomena. *J. Heat Transf.* **2021**, *143*, 120802. [CrossRef]
7. Islamoglu, Y. A new approach for the prediction of the heat transfer rate of the wire-on-tube type heat exchanger—Use of an artificial neural network model. *Appl. Therm. Eng.* **2003**, *23*, 243–249. [CrossRef]

8. Zhao, X. Performance of a Single-Row Heat Exchanger at Low In-Tube Flow Rates. Master's Thesis, University of Notre Dame, Sydney, NSW, Australia, 1995.
9. Peng, H.; Ling, X. Optimal design approach for the plate-fin heat exchangers using neural networks cooperated with genetic algorithms. *Appl. Therm. Eng.* **2008**, *28*, 642–650. [CrossRef]
10. Peng, H.; Ling, X. Neural networks analysis of thermal characteristics on plate-fin heat exchangers with limited experimental data. *Appl. Therm. Eng.* **2009**, *29*, 2251–2256. [CrossRef]
11. Dong, J.T.; Du, Z.Y. Heat exchange quantity prediction of earth-air heat exchanger based on GA-BP neural network. *Renesable Energy Resour.* **2021**, *39*, 307–314.
12. Zhao, F.; Hong, Y.; Yu, D.; Yang, Y. An improved particle swarm optimization based training algorithm for neural network. In *ICMIT 2005: Information Systems and Signal Processing*; SPIE: Bellingham, WA, USA, 2006; Volume 6041, pp. 6–11.
13. Zhang, L.; Zhao, J.; Zhang, X.; Zhang, S. Study of a New Improved PSO-BP Neural Network Algorithm. *J. Harbin Inst. Technol.* **2013**, *20*, 106–112.
14. Wang, J.; Zeng, L.; Yang, K. Multi-objective optimization of printed circuit heat exchanger with airfoil fins based on the improved PSO-BP neural network and the NSGA-II algorithm. *Nucl. Eng. Technol.* **2023**, *55*, 2125–2138. [CrossRef]
15. Chen, Z.; Zheng, D.; Wang, J.; Chen, L.; Sundén, B. Experimental investigation on heat transfer characteristics of various nanofluids in an indoor electric heater. *Renew. Energy* **2020**, *147*, 1011–1018. [CrossRef]
16. Zheng, D.; Yang, J.; Wang, J.; Kabelac, S.; Sundén, B. Analyses of thermal performance and pressure drop in a plate heat exchanger filled with ferrofluids under a magnetic field. *Fuel* **2021**, *293*, 120432. [CrossRef]
17. de Vasconcelos Segundo, E.H.; Mariani, V.C.; dos Santos Coelho, L. Design of heat exchangers using Falcon Optimization Algorithm. *Appl. Therm. Eng.* **2019**, *156*, 119–144. [CrossRef]
18. Wang, D.; Zhang, H.; Wang, G.; Yuan, H.; Peng, X. Experimental and numerical study on the heat transfer and flow characteristics of convex plate heat exchanger based on multi-objective optimization. *Int. J. Heat Mass Transf.* **2023**, *202*, 123755. [CrossRef]
19. Lv, J.; Sun, Y.; Lin, J.; Luo, X.; Li, P. Multi-objective optimization research of printed circuit heat exchanger based on RSM and NSGA-II. *Appl. Therm. Eng.* **2024**, *254*, 123925. [CrossRef]
20. He, Z.; Yu, Q.; Ye, J.; Yan, F.; Li, Y. Optimization of plate-fin heat exchanger performance for heat dissipation of thermoelectric cooler. *Case Stud. Therm. Eng.* **2024**, *53*, 103953. [CrossRef]
21. Yang, H.; Wen, J.; Wang, S.; Li, Y. Thermal design and optimization of plate-fin heat exchangers based global sensitivity analysis and NSGA-II. *Appl. Therm. Eng.* **2018**, *136*, 444–453. [CrossRef]
22. Li, K.; Wen, J.; Wang, S.; Li, Y. Multi-parameter optimization of serrated fins in plate-fin heat exchanger based on fluid-structure interaction. *Appl. Therm. Eng.* **2020**, *176*, 115357. [CrossRef]
23. Kays, W.M.; London, A.L. *Compact Heat Exchangers*; McGraw-Hill: New York, NY, USA, 1984.
24. Dong, J.Q.; Chen, J.P.; Yuan, Q.F.; Chen, Z.J. Flow and Heat Transfer on Compact Smooth Fin Surfaces. *Trans. Chin. Soc. Agric. Mach.* **2007**, *38*, 53–56.
25. BEng, R.G.; Al-Shemmeri, T.T. Thermal and friction factor data for three packed block construction wavy fin surfaces. *Proc. Inst. Mech. Eng. Part A J. Power Energy* **1994**, *208*, 225–229. [CrossRef]
26. Junqi, D.; Jiangping, C.; Zhijiu, C.; Yimin, Z.; Wenfeng, Z. Heat transfer and pressure drop correlations for the wavy fin and flat tube heat exchangers. *Appl. Therm. Eng.* **2007**, *27*, 2066–2073. [CrossRef]
27. Khoshvaght Aliabadi, M.; Gholam Samani, M.; Hormozi, F.; Haghighi Asl, A. 3D-CFD simulation and neural network model for the j and f factors of the wavy fin-and-flat tube heat exchangers. *Braz. J. Chem. Eng.* **2011**, *28*, 505–520. [CrossRef]
28. Qasem, N.A.; Zubair, S.M. Generalized air-side friction and heat transfer correlations for wavy-fin compact heat exchangers. *Int. J. Refrig.* **2019**, *97*, 21–30. [CrossRef]
29. Chang, Y.J.; Wang, C.C. A generalized heat transfer correlation for Iouver fin geometry. *Int. J. Heat Mass Transf.* **1997**, *40*, 533–544. [CrossRef]
30. Wang, C.C.; Chi, K.Y.; Chang, Y.J.; Chang, Y.P. An experimental study of heat transfer and friction characteristics of typical louver fin-and-tube heat exchangers. *Int. J. Heat Mass Transf.* **1998**, *41*, 817–822. [CrossRef]
31. Chang, Y.J.; Hsu, K.C.; Lin, Y.T.; Wang, C.C. A generalized friction correlation for louver fin geometry. *Int. J. Heat Mass Transf.* **2000**, *43*, 2237–2243. [CrossRef]
32. Chang, Y.J.; Chang, W.J.; Li, M.C.; Wang, C.C. An amendment of the generalized friction correlation for louver fin geometry. *Int. J. Heat Mass Transf.* **2006**, *49*, 4250–4253. [CrossRef]
33. Kim, M.H.; Bullard, C.W. Air-side thermal hydraulic performance of multi-louvered fin aluminum heat exchangers. *Int. J. Refrig.* **2002**, *25*, 390–400. [CrossRef]
34. Dong, J.; Chen, J.; Chen, Z.; Zhang, W.; Zhou, Y. Heat transfer and pressure drop correlations for the multi-louvered fin compact heat exchangers. *Energy Convers. Manag.* **2007**, *48*, 1506–1515. [CrossRef]
35. Peng, H.; Ling, X.; Li, J. Performance investigation of an innovative offset strip fin arrays in compact heat exchangers. *Energy Convers. Manag.* **2014**, *80*, 287–297. [CrossRef]

36. Song, R.; Cui, M.; Liu, J. A correlation for heat transfer and flow friction characteristics of the offset strip fin heat exchanger. *Int. J. Heat Mass Transf.* **2017**, *115*, 695–705. [CrossRef]
37. Fisher, R.A. Statistical methods for research workers. In *Breakthroughs in Statistics: Methodology and Distribution*; Springer: New York, NY, USA, 1970; pp. 66–70.
38. Hastie, T.; Tibshirani, R.; Friedman, J. *The Elements of Statistical Learning: Data Mining, Inference, and Prediction*, 2nd ed.; Springer: New York, NY, USA, 2009.
39. Makridakis, S.; Wheelwright, S.C.; Hyndman, R.J. *Forecasting Methods and Applications*; John Wiley & Sons: Hoboken, NJ, USA, 2008.
40. Chen, B.; Zhang, H.; Li, M. Prediction of pK(a) values of neutral and alkaline drugs with particle swarm optimization algorithm and artificial neural network. *Neural Comput. Appl.* **2019**, *31*, 8297–8304. [CrossRef]
41. Kennedy, J.; Eberhart, R. Particle swarm optimization. In *Proceedings of ICNN'95-International Conference on Neural Networks*; IEEE: Piscataway, NJ, USA, 1995; Volume 4, pp. 1942–1948.
42. Bala Sundar Rao, R.; Ranganath, G.; Ranganayakulu, C. Colburn 'j' factor and fanning friction factor 'f' correlations of triangular plain fin surface of a compact heat exchanger using CFD. *Appl. Mech. Mater. Trans. Tech Publ. Ltd.* **2015**, *787*, 207–211. [CrossRef]
43. Ismail, L.S.; Ranganayakulu, C.; Shah, R.K. Numerical study of flow patterns of compact plate-fin heat exchangers and generation of design data for offset and wavy fins. *Int. J. Heat Mass Transf.* **2009**, *52*, 3972–3983. [CrossRef]
44. Ryu, K.; Lee, K.S. Generalized heat-transfer and fluid-flow correlations for corrugated louvered fins. *Int. J. Heat Mass Transf.* **2015**, *83*, 604–612. [CrossRef]
45. Wieting, A.R. Empirical correlations for heat transfer and flow friction characteristics of rectangular offset-fin plate-fin heat exchangers. *J. Heat Transf.* **1975**, *97*, 488. [CrossRef]
46. Joshi, H.M.; Webb, R.L. Heat transfer and friction in the offset stripfin heat exchanger. *Int. J. Heat Mass Transf.* **1987**, *30*, 69–84. [CrossRef]
47. Mochizuki, S.; Yagi, Y.; Yang, W.J. Transport phenomena in stacks of interrupted parallel-plate surfaces. *Exp. Heat Transf. Int. J.* **1987**, *1*, 127–140. [CrossRef]
48. Manglik, R.M.; Bergles, A.E. Heat transfer and pressure drop correlations for the rectangular offset strip fin compact heat exchanger. *Exp. Therm. Fluid Sci.* **1995**, *10*, 171–180. [CrossRef]
49. Kim, M.S.; Lee, J.; Yook, S.J.; Lee, K.S. Correlations and optimization of a heat exchanger with offset-strip fins. *Int. J. Heat Mass Transf.* **2011**, *54*, 2073–2079. [CrossRef]
50. Webb, R.L. Performance evaluation criteria for use of enhanced heat transfer surfaces in heat exchanger design. *Int. J. Heat Mass Transf.* **1981**, *24*, 715–726. [CrossRef]

Disclaimer/Publisher's Note: The statements, opinions and data contained in all publications are solely those of the individual author(s) and contributor(s) and not of MDPI and/or the editor(s). MDPI and/or the editor(s) disclaim responsibility for any injury to people or property resulting from any ideas, methods, instructions or products referred to in the content.